Electric Power Systems Research 248 (2025) 111854

Contents lists available at ScienceDirect

Electric Power Systems Research

journal homepage: www.elsevier.com/locate/epsr

Fractional-order PI control with Modified Stability Locus for grid connected inverters: Stability enhancement and real-time validation

Muhammad Ahsan Zamee, Afaq Hussain *, M.J. Hossain

School of Electrical and Data Engineering, University of Technology Sydney, Sydney, Australia

ARTICLE INFO

Keywords:
Fractional order control
Grid-following inverters
M-SBL approximation
Lyapunov stability
Real-time simulation

ABSTRACT

Conventional proportional–integral (PI) controllers are widely used in grid-connected and islanded inverters, but their fixed gains often yield limited transient response. Fractional-order PI (FOPI) controllers offer improvements by incorporating fractional terms, yet approximating these with first-order ODEs poses challenges, as traditional methods either inflate the system order or compromise accuracy. To overcome these limitations, this paper employs the Modified Stability Boundary Locus (M-SBL) technique, converting fractional expressions into integer-order equivalents while preserving both system order and precision. A generalized inverter model is developed, and fractional orders are optimized using a genetic algorithm, achieving a 25.36% reduction in controller error within 50 iterations. Furthermore, converting the first-order ODE model into a linearized small-signal version reduces computational complexity and accelerates simulations by five times compared to nonlinear methods. Stability is confirmed through eigenvalue analysis and the Lyapunov direct method. Real-time experiments on an OPAL-RT validate the model under dynamic load changes, low voltage ride through (LVRT), voltage sag, and parameter uncertainty conditions.

Grid following inverters (GFLIs) are essential in modern power systems, providing instantaneous real and reactive power support to meet grid demand. Unlike grid forming inverters, which establish voltage and frequency references, GFLIs synchronize to existing grid conditions and inject power accordingly. This capability makes them ideal for integrating renewable energy into a stable grid infrastructure. However, growing GFLI penetration creates challenges in synchronization stability, power quality, and dynamic performance [1]. Accurate control of active and reactive power in the grid following inverters is fundamental to grid stability and efficient power flow: active power balancing maintains frequency within acceptable limits, while reactive power regulation preserves voltage stability margins. As renewable penetration increases, precise power control becomes critical, since inadequate regulation can cause voltage fluctuations and frequency deviations [2].

Control strategies for GFLIs focus on ensuring stable power injection. Conventional PI controllers — widely used in current and voltage loops for their simplicity and effectiveness — struggle with nonlinearities, parameter variations, and dynamic grid conditions [3]. To overcome these limitations, advanced approaches such as model predictive control (MPC) [4], sliding mode control (SMC) [5], and resonant controllers [6] have been proposed. Although these methods yield superior dynamic performance, they incur increased computational complexity. A comprehensive comparison of each strategy's advantages and drawbacks is presented in Table 1.

The integration of grid following inverters (GFLIs) in microgrids underscores the requirement for robust control strategies that adapt to variable grid conditions. Designing effective GFLI controllers remains challenging with both conventional and advanced methods, directly impacting inverter stability in dynamic environments. GFLIs exhibit high sensitivity to grid impedance variations because synchronization relies on grid voltage. Consequently, proportional integral controllers often fail to maintain stability under impedance changes [9]. High penetration of renewable energy reduces grid inertia, further complicating frequency and voltage regulation. Model predictive control and adaptive control [10] mitigate some issues but demand precise system models and substantial computational resources. Moreover, interactions among multiple GFLIs introduce complex dynamics, complicating decentralized controller design for global stability [11]. These challenges underscore the need for innovative solutions to enhance GFLI robustness and adaptability in weak and dynamic grid conditions.

Fractional-order control (FOC) has recently emerged as a promising approach for enhancing performance across various applications [12–15]. Fractional-order PI (FOPI) controllers with anti-windup compensation [16] have demonstrated improved dynamic response and enhanced stability, and can be applicable to grid-following inverters

* Corresponding author.
E-mail addresses: zamee.official@gmail.com (M.A. Zamee), afaq.hussain@student.uts.edu.au (A. Hussain), jahangir.hossain@uts.edu.au (M.J. Hossain).

https://doi.org/10.1016/j.epsr.2025.111854
Received 23 March 2025; Received in revised form 15 May 2025; Accepted 16 May 2025
Available online 9 June 2025

Table 1
Comparison of control strategies for grid-following inverters.

Ref.	Control strategy	Application	Advantages	Limitations
[1]	PLL-based synchronization	Weak grid condition	Robust synchronization	Limited performance in dynamic grids
[2]	Advanced PLL	Renewable energy system	Improved stability	High computational complexity
[3]	Enhanced PI	Weak grid condition	Simple, effective	Poor performance under nonlinear loads
[4]	MPC	Grid-following inverter	Fast dynamic response	Needs accurate model
[5]	SMC	Dynamic performance	Robust to parameter variation	High-frequency oscillations
[6]	Resonant control	Renewable energy system	Harmonic mitigation	Limited frequency adaptability
[7]	FOPI control	Weak grid condition	Improved dynamic response	Needs optimization
[8]	FOC	Weak grid condition	Handles nonlinearity	Complex tuning

(GFLIs) operating under weak grid conditions [7]. Nonetheless, synchronization stability and grid-code compliance during low voltage ride through (LVRT) and voltage sag or swell remain challenging. This paper proposes a novel fractional order approximation-based control strategy to enhance transient response, voltage stability, and dynamic performance.

In the literature, several analytical methods for controller tuning such as Ziegler Nichols, Cohen–Coon, Internal Model Control, Chien–Hrones–Reswick, and pole placement techniques [17] have been widely adopted due to their simplicity and ease of implementation. These methods provide quick initial estimates of controller parameters and are particularly effective for linear time-invariant systems operating under nominal conditions. However, their performance often deteriorates in systems with nonlinear dynamics, parameter uncertainties, or multiple and conflicting control objectives [18]. In contrast, optimization-based tuning methods offer greater flexibility and enhanced performance by systematically adjusting controller gains to meet specific design objectives, such as fast transient response, reduced overshoot, and minimal steady-state error [19]. Consequently, the proposed method in this work employs an optimization-based controller tuning strategy, offering a more efficient and effective alternative to conventional analytical approaches [17].

1. Research gap and key contributions

From Table 1, achieving comprehensive tuning flexibility in fractional-order systems is challenging since their forms are not directly amenable to linear design. Prior studies often rely on nonlinear modeling and hardware implementation, frequently omitting theoretical stability proofs, with exceptions like [7] that employ Oustaloup approximations—which, like other integer-order approximations such as Trigeassou [20], increase the system order and computational time. In the Oustaloup method, the number of poles and zeros increases as 2N+1, where N denotes the approximation order [21]. Similarly, the Trigeassou method requires a high approximation order for accurate representation, thereby increasing the system order, as demonstrated in [20], where an order of 6 was selected for a similar application to this work in inverter control for microgrids. This order increase results in higher computational time. In modern electric grids with thousands of inverter-dominated sources, elevating the order of each system significantly escalates computational demands, imposing additional burdens on computing devices. Another widely used approximation technique is the singularity function method [22], which has been successfully applied in numerous studies and allows flexible system modeling through the selection of singularities (pole-zero pairs), although it typically results in an increased system order. Among integer-order approximation methods that preserve the original system order, continued fraction expansions (CFE) suffer from limited accuracy due to their simplistic form, whereas the modified stability boundary locus (M-SBL) technique [21] precisely maintains system dynamics by fitting stability boundaries with logarithmically spaced sampling points to achieve accurate frequency- and time-domain response matching.

This study applies the M-SBL technique to derive a fully analytical integer-order model of a fractional-order controlled GFLI by converting FOPI controllers, with GA-based tuning yielding faster, smoother transient responses. While this work employs a generalized form of the FOPI controller, the proposed MSBL approach is not limited to this structure. It can be extended to advanced fractional-order designs such as tri-parametric controllers [23,24], FO PI–PD controllers [25], and others, with appropriate adjustments to the system model and approximation order. Stability and performance improvements of the small-signal model versus its nonlinear counterpart are confirmed via the Lyapunov direct method, and experimental validation — including simultaneous and sequential real/reactive power changes, LVRT, and voltage sag tests — demonstrates robust transient performance under switching events and grid disturbances. The main contributions of this study include:

- Developed an accurate linear small-signal model of a fractional-order controlled grid-connected inverter using M-SBL — replacing conventional PI loops in PLL, power, and current control — and optimized fractional orders via GA, with performance validated against the nonlinear model.
- Verified enhanced transient response and stability through eigenvalue and Lyapunov direct analyses, and performed modal characterization (damping ratios, oscillation frequencies, participation factors) to confirm optimal system behavior.
- Demonstrated robust dynamic performance in real-time OPAL-RT simulations under simultaneous and sequential load variations, voltage disturbances (LVRT and voltage sag), and parameter uncertainty.

This paper is organized as follows: Section 2 presents the nonlinear model and full-order small-signal formulation using M-SBL-fitted fractional integrators; Section 3 describes the GA-based optimization of fractional orders for five controllers; Section 4 compares transient response and error metrics of conventional PI versus optimized fractional-order controllers in both nonlinear and linearized models; Section 5 provides a comprehensive stability assessment; Section 6 details real-time OPAL-RT validation under dynamic load switching, grid voltage disturbances, and parameter uncertainty; and Section 7 concludes the paper and outlines directions for future work.

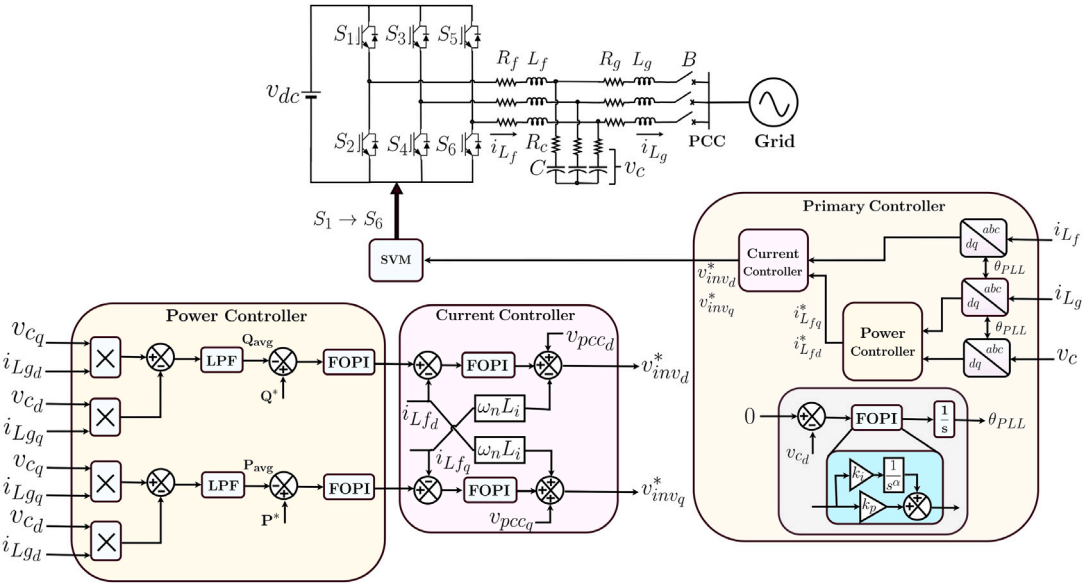

Fig. 1. High-level schematic of the proposed grid connected (Following) inverter system.

2. Mathematical modeling

This study proposes a fractional-order integrator model for a grid-connected inverter operating in grid-following mode to support network balance (see Fig. 1). Initially, a nonlinear state–space representation under conventional PI control is derived. Section 2.2 then presents an M-SBL-based state–space formulation that converts fractional-order controllers into an equivalent integer-order model while preserving the dynamics of fractional integration.

2.1. Nonlinear system modeling under conventional PI controllers

The studied system is a grid-connected inverter interfaced through an RLC filter and controlled by cascaded outer power and inner current loops — both implemented as conventional PI regulators — and a phase-locked loop (PLL) for real-time estimation of grid frequency and phase angle. The following subsections present a detailed description of each subsystem along with their respective mathematical models.

$$P = \frac{3}{2}(v_{c_d} i_{Lg_d} + v_{c_q} i_{Lg_q}), \quad Q = \frac{3}{2}(v_{c_q} i_{Lg_d} - v_{c_d} i_{Lg_q}) \tag{1}$$

In this model, v_{c_d} and v_{c_q} are the d- and q-axis voltages measured at the filter capacitor, while i_{Lg_d} and i_{Lg_q} are the corresponding currents flowing from the filter capacitor node to the grid (PCC). The measured power signals are passed through a low-pass filter to yield the filtered output power:

$$\dot{P_{avg}} = \omega_c \left(P - P_{avg}\right), \quad \dot{Q_{avg}} = \omega_c \left(Q - Q_{avg}\right) \tag{2}$$

Here, ω_c denotes the corner frequency of the low-pass filter. The equations associated with PLL are given as follows:

$$\dot{\beta}_{\text{PLL}} = -v_{c_d}, \quad \dot{\delta} = \omega_{\text{PLL}}, \quad \omega_{\text{PLL}} = \omega_g - (\omega_{ref} + k_p^{\text{PLL}} v_{c_d} + k_i^{\text{PLL}} \beta_{\text{PLL}}) \tag{3}$$

The power controller equations are as follows:

$$\dot{\beta}_d = P_{\text{ref}} - P_{avg}, \quad i_{L_{f_{d_{ref}}}} = k_i^Q \beta_d + k_p^Q \dot{\beta}_d, \quad \dot{\beta}_q = Q_{\text{ref}} - Q_{avg}, \quad i_{L_{f_{q_{ref}}}} = k_i^P \beta_q + k_p^P \dot{\beta}_q \tag{4}$$

In Eqs. (3) and (4), the auxiliary state variable β appears because the preceding integrator converts the original differential expression into an algebraic form. By applying an identical derivation to that used for the voltage controller, the current controller's governing equations are obtained, with Γ serving as the analogous auxiliary state variable. The resulting current controller equations are given below.

$$\dot{\Gamma_d} = i_{L_{f_{d_{ref}}}} - i_{L_{f_d}}, \quad v_{i_{d_{ref}}} = -\omega_{ref} L_f i_{L_{f_q}} + k_i^{c_d} \Gamma_d + k_p^{c_d} \dot{\Gamma_d}, \quad \dot{\Gamma_q} = i_{L_{f_{q_{ref}}}} - i_{L_{f_q}}, \quad v_{i_{q_{ref}}} = \omega_{ref} L_f i_{L_{f_d}} + k_i^{c_q} \Gamma_q + k_p^{c_q} \dot{\Gamma_q} \tag{5}$$

The LCL filter equations are as follows [26]:

$$\begin{aligned}
\dot{i_{L_{f_d}}} &= \frac{1}{L_f}\left(-R_f i_{L_{f_d}} + v_{i_d} - v_{c_d}\right) + \omega_g i_{L_{f_q}}, \\
\dot{i_{L_{f_q}}} &= \frac{1}{L_f}\left(-R_f i_{L_{f_q}} + v_{i_q} - v_{c_q}\right) - \omega_g i_{L_{f_d}}, \\
\dot{i_{Lg_d}} &= \frac{1}{L_g}\left(-R_g i_{Lg_d} + v_{c_d} - v_{pcc_d}\right) + \omega_g i_{Lg_q}, \\
\dot{i_{Lg_q}} &= \frac{1}{L_g}\left(-R_g i_{Lg_q} + v_{c_q} - v_{pcc_q}\right) - \omega_g i_{Lg_d}, \\
\dot{v_{c_d}} &= \frac{1}{C}\left(i_{L_{f_d}} - i_{Lg_d}\right) + \omega_g v_{c_q} + R_C\left(\dot{i_{L_{f_d}}} - \dot{i_{Lg_d}}\right), \\
\dot{v_{c_q}} &= \frac{1}{C}\left(i_{L_{f_q}} - i_{Lg_q}\right) - \omega_g v_{c_d} + R_C\left(\dot{i_{L_{f_q}}} - \dot{i_{Lg_q}}\right)
\end{aligned} \tag{6}$$

A global reference frame transformation must be applied to convert into a local reference frame for the inverter-side calculation.

$$v_{b_d} = \cos(\delta - 0)\, V_{bD} - \sin(\delta - 0)\, V_{bQ}, \quad v_{b_q} = \sin(\delta - 0)\, V_{bD} + \cos(\delta - 0)\, V_{bQ}$$

From the above equations, a system with 14 state variables and a U matrix can be found: $X = [\delta\ P_{avg}\ Q_{avg}\ \beta_d\ \beta_q\ \Gamma_d\ \Gamma_q\ i_{L_{f_d}}\ i_{L_{f_q}}\ v_{c_d}\ v_{c_q}\ i_{Lg_d}\ i_{Lg_q}\ \beta_{\text{PLL}}]$ and $U = [P_{ref}\ Q_{ref}\ V_{bD}\ V_{bQ}\ \omega_g]$

Section 2.2 presents a fractional-order modeling approach using the M-SBL fitting method, replacing conventional PI controllers with FOPI controllers to achieve superior dynamic response and control precision.

2.2. Fractional-order approximation using MSBL fitting and proposed system model

An approximate transfer function is derived based on the M-SBL framework [21]. Let ϕ denote the fractional order of differentiation, and let M represent the order of an integer-based approximation. The parameters Ω_{low} and Ω_{high} are designated as the lower and upper-frequency bounds, respectively. The derivation is carried out through the following steps.

1. Logarithmic frequency allocation

A set of M logarithmically spaced frequencies, $\{\Omega(q)\}$ for $q = 1, \ldots, M$, is introduced over the interval $[\Omega_{\text{low}}, \Omega_{\text{high}}]$. Two cases arise and are arranged to ensure broad coverage of the frequency range with manageable computational effort.

$$\Omega(q) = \begin{cases} \Omega_{\text{high}}, & \text{if } M = 1, \\ \Omega_{\text{low}} \left(\dfrac{\Omega_{\text{high}}}{\Omega_{\text{low}}} \right)^{\frac{q-1}{M-1}}, & \text{if } M > 1, \quad q = 1, \ldots, M. \end{cases}$$

2. Construction of system matrices

A matrix $\mathbf{X}$ and a vector $\mathbf{Y}$ are then constructed to capture the real and imaginary components of the fractional operator's response. Let p and q range from 1 to M. The entries of $\mathbf{X}$ are determined by

$$X(p,q) = \left(i\,\Omega(q)\right)^{p} - \left(i\,\Omega(q)\right)^{M-p+2} \frac{\cos\left(\frac{\pi}{2}\phi\right)}{\Omega(q)^{\phi}} - \left(i\,\Omega(q)\right)^{M-p+1} \frac{\sin\left(\frac{\pi}{2}\phi\right)}{\Omega(q)^{\phi-1}},$$

where i is the imaginary unit. Real and imaginary parts are combined into a single real-valued expression for each pair (p, q). For each $q \in \{1, \ldots, M\}$, the entries of $\mathbf{Y}$ are given by $Y(1,q) = -(i\,\Omega(q))^{M+1} + (i\,\Omega(q))\frac{\cos\left(\frac{\pi}{2}\phi\right)}{\Omega(q)^{\phi}} + \frac{\sin\left(\frac{\pi}{2}\phi\right)}{\Omega(q)^{\phi-1}}$. Once again, real and imaginary parts are summed to form the final real-valued entries.

3. Determination of approximation coefficients

After $\mathbf{X}$ and $\mathbf{Y}$ have been assembled, the coefficient vector $\boldsymbol{Z}$ (of dimension M) is determined by $\boldsymbol{Z} = (\mathbf{X}^{-1})^T \mathbf{Y}^T$, thus storing the numeric coefficients required to form the approximation.

4. Form of the approximate transfer function

Using $\boldsymbol{Z} = [Z_1, Z_2, \ldots, Z_M]^T$, the approximate transfer function's numerator coefficients are $[Z_1, Z_2, \ldots, Z_M, 1]$ and its denominator coefficients are $[1, Z_M, Z_{M-1}, \ldots, Z_2, Z_1]$. The resulting fractional-order approximation is denoted by

$$H_{\text{approx}}(s) = \frac{Z_1\, s^M + Z_2\, s^{M-1} + \ldots + Z_M\, s + 1}{s^M + Z_M\, s^{M-1} + \ldots + Z_2\, s + Z_1}.$$

5. State–space realization

A controllable canonical form can be obtained from the polynomials above. It is given by: $A_{\text{Frac}} = [[-Z_M, -Z_{M-1}, \ldots, -Z_1]; I_{(M-1)}]$, $B_{\text{Frac}} = [1, 0, \ldots, 0]^T$, $C_{\text{Frac}} = [Z_1, Z_2, \ldots, Z_M, 1]$, $D_{\text{Frac}} = 0$.

Here, $\mathbf{I}_{(M-1)}$ denotes the $(M-1)\times(M-1)$ identity matrix. For an M-dimensional realization, the state variables $\{X_{\text{Frac},1}, X_{\text{Frac},2}, \ldots, X_{\text{Frac},M}\}$ are defined, and their dynamics are governed by

$$\dot{X}_{\text{Frac},1} = \sum_{j=1}^{M} A_{\text{Frac},1j}\, X_{\text{Frac},j} + U_{\text{Frac}}, \quad \dot{X}_{\text{Frac},k} = X_{\text{Frac},k-1}, \quad k = 2, \ldots, M.$$

where U_{Frac} is the input to this fractional-element model and the output is given by $Y_{\text{Frac}} = C_{\text{Frac}}\left[X_{\text{Frac},1}, X_{\text{Frac},2}, \ldots, X_{\text{Frac},M}\right]^{\mathsf{T}} + D_{\text{Frac}}\, U_{\text{Frac}}$.

Using the Mth-order approximation eliminates the need for conventional integrators by treating auxiliary state variables (e.g., from the PLL, power, and current loops) as inputs to the fractional operator, thereby preserving the original system dimension while substituting integer-order integration with its fractional equivalent. An $M = 1$ approximation retains the original order, whereas larger M values add internal states only to capture fractional dynamics. Consequently, the system can be compactly written as: $\dot{X} = AX + BU$. This 14th-order model is then linearized to derive its Jacobian matrix, the non-zero entries of which follow using auxiliary variables for clarity.

$$\begin{aligned} T^{X}_{1_\alpha} = {} & \text{imag}(w_h^2) + \text{real}(w_h^2) - \text{imag}(w_h^{1-\alpha_X}\cos(\tfrac{\pi}{2}\alpha_X)) \\ & + \text{real}(w_h^{1-\alpha_X}\cos(\tfrac{\pi}{2}\alpha_X)) \\ & + \text{imag}(w_h^{1-\alpha_X}\sin(\tfrac{\pi}{2}\alpha_X)) + \text{real}(w_h^{1-\alpha_X}\sin(\tfrac{\pi}{2}\alpha_X)) \end{aligned}$$

$$\begin{aligned} T^{X}_{2_\alpha} = {} & \text{imag}(w_h^{2-\alpha_X}\cos(\tfrac{\pi}{2}\alpha_X)) + \text{real}(w_h^{2-\alpha_X}\cos(\tfrac{\pi}{2}\alpha_X)) \\ & + \text{imag}(w_h^{2-\alpha_X}\sin(\tfrac{\pi}{2}\alpha_X)) \\ & - \text{real}(w_h^{2-\alpha_X}\sin(\tfrac{\pi}{2}\alpha_X)) - \text{imag}(w_h) + \text{real}(w_h) \end{aligned}$$

where X is P, Q, PLL, $i_{L_{f_d}}$, or $i_{L_{f_q}}$, depending on the actual equation. The entries in the following are represented together in terms of similarity.

$$a_{2,2} = a_{3,3} = -\omega_c, \quad a_{2,8} = a_{3,9} = 1.5\, i_{\text{Lg}_\text{d}}\, \omega_c, \quad a_{2,13} = a_{3,12} = 1.5\, v_{\text{c}_\text{q}}\, \omega_c$$

$$a_{4,2} = a_{5,3} = a_{6,10} = a_{7,11} = a_{14,8} = -1, \quad a_{i,i} = -\frac{T^{X_i}_{1_\alpha}}{T^{X_i}_{2_\alpha}}, \quad i = 4,5,6,7,14$$

where $X_4 = P$, $X_5 = Q$, $X_6 = i_{L_{f_d}}$, $X_7 = i_{L_{f_q}}$, $X_{14} = \text{PLL}$

$$a_{2,9} = -a_{3,8} = 1.5\, i_{\text{Lg}_\text{q}}\, \omega_c, \quad a_{2,12} = -a_{3,13} = 1.5\, \omega_c\, \text{v}_{\text{c}_\text{d}},$$

$$a_{8,11} = -a_{9,10} = \text{R}_\text{C}\left(\omega_g - \omega_n\right),$$

$$a_{8,13} = -a_{9,12} = -\,\text{R}_\text{C}\,\omega_g, \quad a_{10,11} = -a_{11,10} = \omega_g - \omega_n,$$

$$a_{12,13} = -a_{13,12} = \omega_g,$$

$$a_{8,8} = a_{9,9} = -\text{R}_\text{C}\left(\frac{1}{\text{L}_\text{g}} + \frac{1}{\text{L}_\text{f}}\right), \quad a_{8,9} = a_{9,8} = a_{12,13} = \omega_g$$

$$a_{8,12} = a_{9,13} = \frac{\text{R}_\text{C}\,\text{R}_\text{g}}{\text{L}_\text{g}} - \frac{1}{\text{C}}, \quad a_{10,8} = a_{11,9} = -\frac{1}{\text{L}_\text{f}}, \quad a_{12,8} = a_{13,9} = \frac{1}{\text{L}_\text{g}},$$

$$a_{12,12} = a_{13,13} = -\frac{\text{R}_\text{g}}{\text{L}_\text{g}}, \quad a_{1,8} = k_p^{\text{PLL}} + \frac{k_i^{\text{PLL}}\, T^{\text{PLL}}_{1,\alpha}}{T^{\text{PLL}}_{2,\alpha}}$$

$$a_{8,3} = -b_{8,2} = -\frac{R_C}{L_f}\left\{k_p^Q + \frac{k_i^Q\, T^Q_{1,\alpha}}{T^Q_{2,\alpha}}\right\}\left[k_p^{c_d} + k_i^{c_d}\frac{T^{\text{ild}}_{1,\alpha}}{T^{\text{ild}}_{2,\alpha}}\right]$$

$$a_{9,2} = -b_{9,1} = -\frac{R_C}{L_f}\left\{k_p^P + \frac{k_i^P T^P_{1,\alpha}}{T^P_{2,\alpha}}\right\}\left[k_p^{c_q} + k_i^{c_q}\frac{T^{\text{ilq}}_{1,\alpha}}{T^{\text{ilq}}_{2,\alpha}}\right]$$

$$a_{10,3} = -b_{10,2} = -\frac{1}{L_f}\left\{k_p^Q + \frac{k_i^Q\, T^Q_{1,\alpha}}{T^Q_{2,\alpha}}\right\}\left[k_p^{c_d} + k_i^{c_d}\frac{T^{\text{ild}}_{1,\alpha}}{T^{\text{ild}}_{2,\alpha}}\right]$$

$$a_{11,2} = -b_{11,1} = -\frac{1}{L_f}\left\{k_p^P + \frac{k_i^P\, T^P_{1,\alpha}}{T^P_{2,\alpha}}\right\}\left[k_p^{c_q} + k_i^{c_q}\frac{T^{\text{ilq}}_{1,\alpha}}{T^{\text{ilq}}_{2,\alpha}}\right]$$

$$a_{8,5} = -\frac{k_i^Q R_C}{L_f}\left\{\frac{(T^Q_{1,\alpha})^2}{(T^Q_{2,\alpha})^2} - 1\right\}\left[k_p^{c_d} + k_i^{c_d}\frac{T^{\text{ild}}_{1,\alpha}}{T^{\text{ild}}_{2,\alpha}}\right],$$

$$a_{10,5} = -\frac{k_i^Q}{L_f}\left\{\frac{(T^Q_{1,\alpha})^2}{(T^Q_{2,\alpha})^2} - 1\right\}\left[k_p^{c_d} + k_i^{c_d}\frac{T^{\text{ild}}_{1,\alpha}}{T^{\text{ild}}_{2,\alpha}}\right]$$

$$a_{9,4} = -\frac{k_i^P R_C}{L_f}\left\{\frac{(T^P_{1,\alpha})^2}{(T^P_{2,\alpha})^2} - 1\right\}\left[k_p^{c_q} + k_i^{c_q}\frac{T^{\text{ilq}}_{1,\alpha}}{T^{\text{ilq}}_{2,\alpha}}\right],$$

$$a_{11,4} = -\frac{k_i^P}{L_f}\left\{\frac{(T^P_{1,\alpha})^2}{(T^P_{2,\alpha})^2} - 1\right\}\left[k_p^{c_q} + k_i^{c_q}\frac{T^{\text{ilq}}_{1,\alpha}}{T^{\text{ilq}}_{2,\alpha}}\right]$$

$$a_{8,10} = \frac{1}{\text{C}} - \frac{\text{R}_\text{C}}{\text{L}_\text{f}}\left(k_p^{c_d} + \text{R}_\text{f} + \frac{k_i^{c_d}\, T^{\text{ild}}_{1,\alpha}}{T^{\text{ild}}_{2,\alpha}}\right),$$

$$a_{9,11} = \frac{1}{\text{C}} - \frac{\text{R}_\text{C}}{\text{L}_\text{f}}\left(k_p^{c_q} + \text{R}_\text{f} + \frac{k_i^{\text{c}_\text{q}}\, T^{\text{ilq}}_{1,\alpha}}{T^{\text{ilq}}_{2,\alpha}}\right)$$

$$a_{10,10} = -\frac{1}{\mathrm{L_f}}\left(k_p^{c_d} + \mathrm{R_f} + \frac{k_i^{c_d} T_{1,\alpha}^{\mathrm{ild}}}{T_{2,\alpha}^{\mathrm{ild}}}\right),$$

$$a_{11,11} = -\frac{1}{\mathrm{L_f}}\left(k_p^{c_q} + \mathrm{R_f} + \frac{k_i^{\mathrm{c_q}} T_{1,\alpha}^{\mathrm{ilq}}}{T_{2,\alpha}^{\mathrm{ilq}}}\right)$$

$$a_{1,14} = k_i^{\mathrm{PLL}}\left[\frac{\left(T_{1,\alpha}^{\mathrm{PLL}}\right)^2}{\left(T_{2,\alpha}^{\mathrm{PLL}}\right)^2} - 1\right], \quad a_{6,5} = -k_i^{Q}\left[\frac{\left(T_{1,\alpha}^{Q}\right)^2}{\left(T_{2,\alpha}^{Q}\right)^2} - 1\right],$$

$$a_{7,4} = -k_i^{P}\left[\frac{\left(T_{1,\alpha}^{P}\right)^2}{\left(T_{2,\alpha}^{P}\right)^2} - 1\right],$$

$$a_{8,6} = -\frac{k_i^{c_d}\,\mathrm{R_C}}{\mathrm{L_f}}\left[\frac{\left(T_{1,\alpha}^{\mathrm{ild}}\right)^2}{\left(T_{2,\alpha}^{\mathrm{ild}}\right)^2} - 1\right], \quad a_{10,6} = -\frac{k_i^{\mathrm{c_d}}}{L_{\mathrm{f}}}\left[\frac{\left(T_{1,\alpha}^{\mathrm{ild}}\right)^2}{\left(T_{2,\alpha}^{\mathrm{ild}}\right)^2} - 1\right],$$

$$a_{9,7} = -\frac{k_i^{\mathrm{c_q}} R_{\mathrm{c}}}{L_{\mathrm{f}}}\left[\frac{\left(T_{1,\alpha}^{\mathrm{ilq}}\right)^2}{\left(T_{2,\alpha}^{\mathrm{ilq}}\right)^2} - 1\right]$$

$$a_{11,7} = -\frac{k_i^{\mathrm{c_q}}}{L_{\mathrm{f}}}\left[\frac{\left(T_{1,\alpha}^{\mathrm{ilq}}\right)^2}{\left(T_{2,\alpha}^{\mathrm{ilq}}\right)^2} - 1\right], \quad a_{6,3} = -\left[k_p^{\mathrm{Q}} + \frac{k_i^{\mathrm{Q}} T_{1,\alpha}^{\mathrm{Q}}}{T_{2,\alpha}^{\mathrm{Q}}}\right],$$

$$a_{7,2} = -\left[k_p^{\mathrm{P}} + \frac{k_i^{\mathrm{P}} T_{1,\alpha}^{\mathrm{P}}}{T_{2,\alpha}^{\mathrm{P}}}\right]$$

$$a_{8,1} = -Ra_{12,1} = -\frac{\mathrm{R}}{\mathrm{Lc}}\left(V_{\mathrm{bQ}}\cos\delta + V_{\mathrm{bD}}\sin\delta\right),$$

$$a_{9,1} = -Ra_{13,1} = \frac{\mathrm{R}}{\mathrm{Lc}}\left(V_{\mathrm{bD}}\cos\delta - V_{\mathrm{bQ}}\sin\delta\right)$$

The input B matrix entries can be represented as:

$$b_{4,1} = b_{5,2} = 1, \quad b_{8,3} = b_{9,4} = \frac{R_c\cos(\delta)}{L_c}, \quad b_{12,3} = b_{13,4} = -\frac{\cos(\delta)}{L_c},$$

$$b_{8,4} = -\frac{R_c\sin(\delta)}{L_c},$$

$$b_{9,3} = \frac{R_c\sin(\delta)}{L_c}, \quad b_{13,3} = -\frac{\sin(\delta)}{L_c}, \quad b_{12,4} = \frac{\sin(\delta)}{L_c}, \quad b_{11,5} = -i_{Lf_d},$$

$$b_{13,5} = -i_{Lg_d},$$

$$b_{6,2} = k_p^{Q} + \frac{k_i^{Q} T_{1,\alpha}^{Q}}{T_{2,\alpha}^{Q}}, \quad b_{7,1} = k_p^{P} + \frac{k_i^{P} T_{1,\alpha}^{P}}{T_{2,\alpha}^{P}}, \quad b_{8,5} = v_{c_q} + R_c\,(i_{Lf_q} - i_{Lg_q}),$$

$$b_{9,5} = v_{c_d} - R_c\,(i_{Lf_d} - i_{Lg_d}), \quad b_{10,5} = i_{Lf_q}, \quad b_{12,5} = i_{Lg_q}$$

A GA is employed to optimize the fractional orders of the controllers for optimal model performance, as detailed in the next section.

3. GA-driven tuning of controller parameters

Tuning the integrators' fractional orders is shown to improve system performance. PI gains and key system parameters are adopted from [26,27] (nominal values listed in the Appendix). The five fractional-order exponents in the model are then optimized using a genetic algorithm, as detailed in the pseudocode. It should be noted that in this work, the adopted PI controller gain parameters are kept constant [26–28]; only the fractional orders were optimized, demonstrating that significant improvements in stability can be achieved even when the PI gains are fixed. The GA initializes by defining the system, fractional-order bounds, and a five dimensional search space for α_P, α_Q, $\alpha_{i_{Lf_d}}$, $\alpha_{i_{Lf_q}}$, and α_{PLL}. A population is randomly generated within the specified lower (lb) and upper (ub) limits, with fixed crossover, mutation, and elitism rates. For each candidate, the FOPI model is constructed via the M-SBL(α, N, w_b, w_h) method discussed in 2.2 and both nonlinear and small-signal Simulink simulations are executed. The fitness function combines the integral time-absolute error (ITAE) of the PLL, inductor currents, and active/reactive power loops with penalty terms quantifying mismatches in P, Q, v_{c_q}, and ω_{PLL}; infeasible solutions incur infinite fitness. Although GA is a well-established optimization method, including fractional-order applications [15], it is uniquely applied in this work by designing a fitness function that simultaneously minimizes the ITAE and the error between linear and nonlinear model responses, enabling the development of a reliable linear model closely matching the nonlinear system. Successive generations are produced via roulette-wheel selection, single-point crossover, mutation, and elitism. Upon completion of the prescribed number of generations, the GA returns the optimal fractional orders and their fitness value. Fig. 2 shows the convergence of the five fractional orders ($\alpha_P, \alpha_Q, \alpha_{i_{Lf_d}}, \alpha_{i_{Lf_q}}, \alpha_{PLL}$) and the objective function over 50 GA generations, starting from bounds of −5 to −0.1.

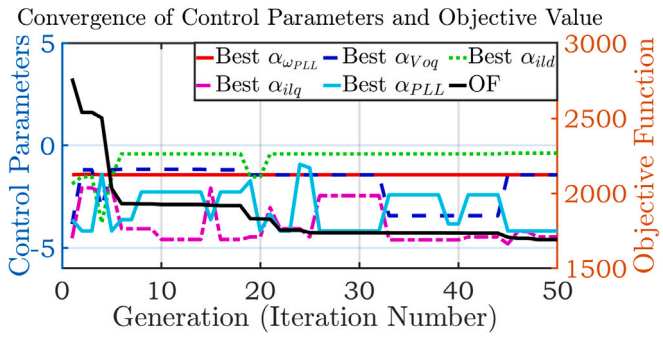

Fig. 2. Controller parameters and objective function convergence diagram.

Algorithm 1 GA-based Optimization for FOPI Controller Parameters

Initialization:
– Define system parameters, state variables
Initialize FOPI limits $N = 1$, $w_b = 0.001$, $w_h = 1000$; set fractional-order bounds $lb = -5$, $ub = -0.1$; configure GA with *population_size* = 50, *max_iter* = 50, *dim* = 5, *crossover_rate* = 0.8, *mutation_rate* = 0.2, *elite_count* = 1; generate initial population uniformly in $[lb, ub]^{dim}$; set *global_best_fitness* ← ∞.
for $g \leftarrow 1$ to *max_iter* **do**
  Fitness Evaluation:
  for $i \leftarrow 1$ to *population_size* **do**
    Extract $(\alpha_P, \alpha_Q, \alpha_{ild}, \alpha_{ilq}, \alpha_{PLL})$ from *population*[i]
    Build FOPI models via *M-SBL*(α, N, w_b, w_h), simulate nonlinear and linearized models, and compute $\mathrm{ITAE}_{sum} = \mathrm{ITAE}_{PLL} + \mathrm{ITAE}_{id} + \mathrm{ITAE}_{iq} + \mathrm{ITAE}_{P} + \mathrm{ITAE}_{Q}$.
    if valid **then**
      $fitness[i] \leftarrow \mathrm{ITAE}_{sum} + \sum |P_{\mathrm{nonlin}} - P_{\mathrm{lin}}| + \sum |Q_{\mathrm{nonlin}} - Q_{\mathrm{lin}}| + \sum |V_{c_q,\mathrm{nonlin}} - V_{c_q,\mathrm{lin}}| + \sum |\omega_{\mathrm{PLL,nonlin}} - \omega_{\mathrm{PLL,lin}}|$
    else $fitness[i] \leftarrow \infty$
    end if
  end for
  Update Global Best:
  best_idx ← arg min(*fitness*), *current_best* ← min(*fitness*)
  if *current_best* < *global_best_fitness* **then**
    global_best_fitness ← *current_best*, *global_best_position* ← *population*[*best_idx*]
  end if
  GA Operators (Selection, Crossover, Mutation, Elitism):
  Convert fitness to scores = $1/(fitness+\epsilon)$; perform roulette-wheel selection
  Preserve top *elite_count*, apply single-point crossover with prob. *crossover_rate*
  Mutate genes with prob. *mutation_rate*; enforce bounds $[lb, ub]$
end for
Output: Return *global_best_position* and *global_best_fitness*

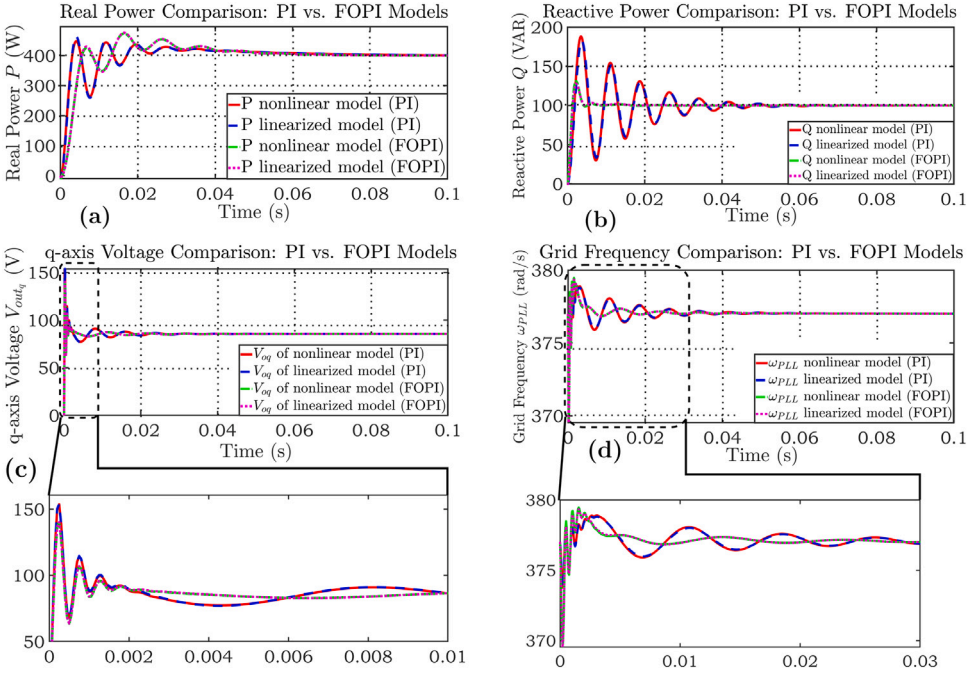

Fig. 3. Performance comparison of nonlinear and linearized model under PI and FOPI control: (a) Real power, (b) Reactive power, (c) q-axis voltage, and (d) Grid frequency.

Table 2
Optimized control parameters and corresponding error.

Optimal fractional order					Error
α_P	α_Q	$\alpha_{i_{Lf_d}}$	$\alpha_{i_{Lf_q}}$	α_{PLL}	Fitness value
−1.4291	−1.4337	−0.3738	−4.4688	−4.1725	1.6923×10^3

All parameters converge within 50 iterations, with optimal values reported in Table 2, and the objective function reaching $1.6923{\times}10^3$. Using these optimized settings, the FOPI controller achieves an $ITAE_{sum}$ of 0.0574 — 25.36% lower than the 0.0769 error of the conventional PI design — demonstrating the clear performance advantage of the fractional-order approach.

4. Comparison of conventional PI and GA-optimized FOPI controller performance

A comparative analysis of the nonlinear and small-signal models for both PI- and FOPI-based controllers — using the optimally tuned parameters — evaluates their effectiveness in stabilizing voltage, angular frequency, and real/reactive power. The results are shown in Fig. 3 and summarized in Table 3.

Table 3 summarizes transient metrics for PI versus FOPI controllers across real power, reactive power, q-axis voltage, and angular frequency. For real power, the PI controller achieves lower overshoot (12.03% vs. 18.34%) and a marginally faster rise time (0.002 s vs. 0.003 s), whereas the FOPI controller settles faster (0.051 s vs. 0.060 s). In reactive power, FOPI markedly outperforms PI—reducing overshoot from 88.05% to 31.22% and settling in 0.007 s versus 0.050 s (rise time identical at 0.001 s). Similarly, q-axis voltage overshoot is lower with FOPI (64.02% vs. 79.82%) and settles quicker (0.012 s vs. 0.017 s), with negligible difference in rise time in order of 10^{-5} s. Neither controller exhibits appreciable settling time for angular frequency, though PI attains a slightly lower overshoot (0.5032% vs. 0.652%). Overall, FOPI delivers superior transient performance across three of four criteria. Moreover, the small-signal model accurately replicates nonlinear dynamics while requiring only 1.1354 s to simulate one second of operation — nearly five times faster than the nonlinear model's 5.3696 s on an 11th-Gen Intel® Core™ i5-1135G7 with 16 GB RAM — making it highly advantageous for large-scale simulations.

5. Stability and modal analysis: A thorough exploration

In addition to numerical validation, analytical stability of the optimized system is confirmed via eigenvalue analysis and the Lyapunov direct method; Tables 4 and 5 detail eigenvalues, damping ratios, natural frequencies, and principal state contributions for each mode, providing a comprehensive stability characterization of the proposed model.

Table 4 identifies five oscillatory modes (indices 1–10). Modes 1 and 2 operate at very high frequencies (on the order of 1.9–193 kHz) with large negative real parts (−2461.03 and −2295.97 s^{-1}) and moderate damping ratios (20.29% and 18.86%), indicating rapid decay despite underdamping; they are dominated by v_{c_d}, v_{c_q}, and i_{Lg_d}. Modes 3 and 4 (indices 5–8) occur at 245 Hz and 99.47 Hz with damping ratios of 44.62% (driven by Q_{avg} and i_{Lg_d}) and 13.43% (linked to P_{avg}), respectively—Mode 4 is the least damped but remains stable. Mode 5 (indices 9–10) appears at 2.08 Hz with a high damping ratio of 82.08% (real part –10.73, imaginary 7.47), associated with v_{c_d} and Q_{avg}. Table 5 lists four purely real modes (indices 11–14) with real parts from –15.46 to –96.86 s^{-1} and 100% damping, confirming non-oscillatory decay. In this work, the system stability is demonstrated through eigenvalue analysis, with Tables 4 and 5 showing that all eigenvalues of the system matrix A have negative real parts, confirming that A is a Hurwitz matrix. Consequently, for any positive definite matrix Q (e.g., the identity matrix), the Lyapunov condition $A^TP + PA = -Q$ admits a unique positive definite solution P, which can be readily obtained using computational tools such as MATLAB's built-in lyap function. This guarantees asymptotic convergence. Experimental validation under dynamic load, voltage disturbances, and parameter uncertainty is presented in the next section.

6. Experimental results

Model performance was validated via hardware-in-the-loop (HIL) experiments. As shown in Fig. 4, the setup comprises an OPAL-RT OP5707 real-time digital simulator, a measurement system, and a PC

Table 3
Comparative analysis of PI and FOPI controllers based on transient indicators.

Controller type	Transient indicator	Real power	Reactive power	q-Axis voltage	Angular frequency
PI	Overshoot (%)	12.031	88.047	79.823	0.503
PI	Settling Time (s)	0.060	0.050	0.017	0
PI	Rise Time (s)	0.002	0.001	8.2e−05	0
FOPI	Overshoot (%)	18.342	31.222	64.021	0.652
FOPI	Settling Time (s)	0.051	0.007	0.012	0
FOPI	Rise Time (s)	0.003	0.001	8.9e−05	0

Table 4
Analysis of eigenvalues with non-zero imaginary parts.

Index (mode)	Real (1/s)	Imaginary (rad/s)	Damping ratio(%)	Natural frequency (Hz)	Major participants
1,2 (1)	−2461.03	11 876.45	20.29	193 035	v_{c_d}, i_{Lg_d}, v_{c_q}
3,4 (2)	−2295.97	11 955.23	18.86	1937.50	v_{c_d}, v_{c_q}, i_{Lg_d}
5,6 (3)	−687.17	1378.15	44.62	245.09	Q_{avg}, i_{Lg_d}, i_{Lf_d}, v_{c_d}
7,8 (4)	−83.96	619.32	13.43	99.47	P_{avg}
9,10 (5)	−10.73	7.47	82.08	2.08	v_{c_d}, Q_{avg}

Table 5
Analysis of eigenvalues with no imaginary parts.

Index	Real (1/s)	Damping ratio (%)	Natural frequency (Hz)
11	−15.46	100.00	2.46
12	−96.86	100.00	15.42
13	−95.98	100.00	15.28
14	−90.11	100.00	14.34

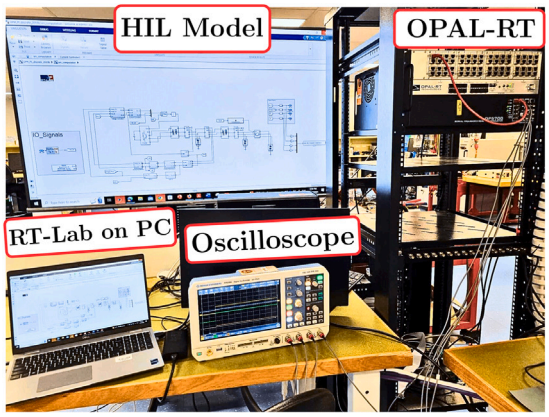

Fig. 4. Laboratory experimental setup.

for real-time data exchange. The model was evaluated under four scenarios: (1) simultaneous changes in active and reactive power (P and Q); (2) sequential P and Q variations introduced at different times; (3) voltage disturbances, including LVRT and voltage sag; and (4) parameter uncertainty. Detailed descriptions of each scenario and their results are presented in the following subsections.

6.1. Simultaneous dynamic load variation

The system's transient response was evaluated at startup and during a load step at 6.8 s — raising real power demand from 400 W to 800 W and reactive power from 200 VAR to 420 VAR — while grid frequency (ω_{PLL}), q-axis voltage (v_{c_q}), and real/reactive power. Data from the OPAL-RT simulator were captured on an oscilloscope, Gaussian-filtered, and plotted in MATLAB (Fig. 5). The PLL frequency settled in just 2 ms with a 0.674% overshoot, demonstrating exceptionally fast damping. In contrast, v_{c_q}, real power P, and reactive power Q each required approximately 6.83–6.86 s to reach steady state; their overshoots were 10.08%, $< 2\%$, and 26.84%, respectively, indicating fast and satisfying transient behavior. Despite these differences, all variables converged without instability, confirming robust dynamic performance.

Also, the proposed FOPI controller demonstrates superior performance compared to the conventional PI controller. Both controllers achieve similar angular frequency responses, with the PI controller exhibiting a settling time of approximately 2 ms and an overshoot of 0.5126%. However, the FOPI controller outperforms the PI controller in regulating real power (P), reactive power (Q), and voltage (v_{c_q}). Specifically, the PI controller results in an 18.77% overshoot in P, whereas the FOPI controller maintains it below 2%. For Q, the PI controller's overshoot reaches 57.86%, significantly higher than the FOPI controller's 26.84%. In terms of voltage regulation, the PI controller exhibits an overshoot of 11.13%, slightly exceeding the FOPI controller's 10.08%. Given that higher overshoot can lead to prolonged settling times, oscillatory transients, and increased stress on system components, the FOPI controller's lower overshoot underscores its enhanced transient robustness and reliability over PI-based controllers.

6.2. Sequential dynamic load variation

For sequential dynamic load variation, load changes are made around 4.75 s (reactive power) and 7.78 s (real power). The change in load level is the same as in the previous case. The results indicate an exceptionally fast response in ω, with a rise time of 0.0017 s and a notably small overshoot of only 0.5571%. By comparison, v_{c_q} requires 4.79 s to settle and experiences a moderate overshoot of 5.52%. Real power P settles in about 7.78 s and has a modest overshoot of 0.9992%, whereas reactive power Q reaches steady-state in roughly 4.80 s yet incurs the largest overshoot at 23.81%. Notably, ω and v_{c_q} share relatively fast rise times (on the order of milliseconds and just under two milliseconds, respectively), while P and Q transition more slowly. However, Q exhibits more significant oscillatory behavior due to its higher overshoot. Overall, each variable stabilizes without significant unusual transient behavior, suggesting a well-controlled system but with Q warranting closer damping considerations.

The proposed FOPI controller also demonstrates superior performance over the PI controller under sequential load changes. While both controllers exhibit similar rise times for angular frequency, the

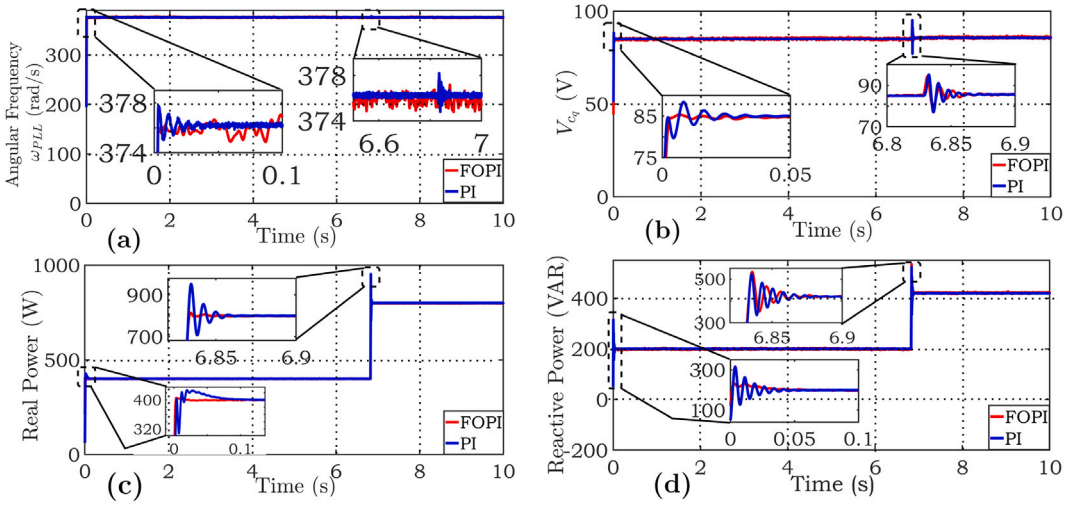

Fig. 5. Performance of the FOPI-based model during simultaneous dynamically varied load conditions: (a) angular frequency, ω_{PLL}, (b) q-Axis voltage v_{c_q}, (c) Real power P, and (d) Reactive power Q.

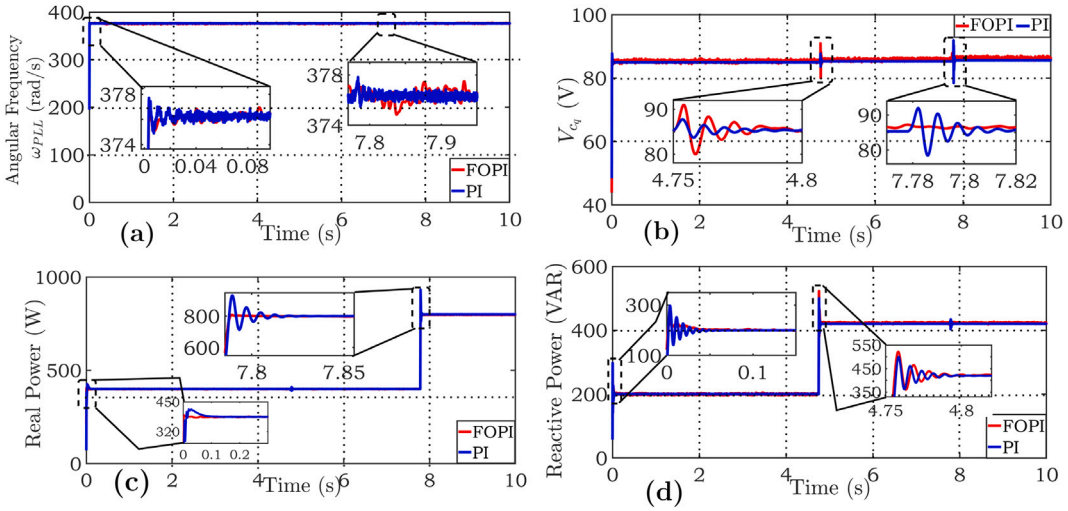

Fig. 6. Performance of the FOPI-based model during arbitrary time, dynamically varied load conditions: (a) Angular frequency ω_{PLL}, (b) q-Axis voltage v_{c_q}, (c) Real power P, and (d) Reactive power Q.

PI controller shows a higher overshoot of 0.7493%. For real power, reactive power, and voltage, the FOPI controller achieves significantly lower overshoots of 0.999%, 23.81%, and 5.52%, respectively, compared to 16.40%, 48.71%, and 7.40% observed with the PI controller. Additionally, although the rise times for angular frequency are the same, the FOPI controller attains improved settling performance in voltage (4.79 s versus 7.79 s) and real power (7.78 s versus 7.79 s), further highlighting its enhanced transient response and reliability (see Fig. 6).

6.3. Voltage variation

For the LVRT and voltage sag test, complete voltage shutdown was provided at around 4.84 s and kept for 100 ms, whereas 15% voltage sag has provided at around 7.85 and again kept for 100 ms (see Fig. 7).

The step responses exhibit distinctly different dynamics for the four variables. Notably, ω settles almost immediately within 2 ms—with minimal overshoot (0.47%) and no undershoot. Real power P also responds very rapidly, boasting a rise time of just 0.0015 s, although it registers a modest overshoot of 2.38%. By contrast, v_{c_q} requires nearly 8 s to settle and, while it sees only a moderate 4.61% overshoot, it undergoes a 6.85% undershoot. Reactive power Q combines a relatively fast initial rise (0.0013 s) with a prolonged settling period of nearly 5 s and the largest overshoot at 30.75%. Overall, ω and P appear tightly controlled and highly responsive, whereas v_{c_q} and especially Q are more prone to oscillatory behavior, warranting further tuning or damping measures.

6.4. Parameter uncertainty

Under this scenario, the line filter parameters were varied by +10% and −10% from their nominal values, as listed in Appendix. Simulations were conducted with reference real and reactive powers of 800 W and 400 VAR, respectively (Fig. 8). In both parameter variation cases, the system achieved steady state rapidly. The settling times for real power, reactive power, and voltage ranged from 0.0038 s (reactive power at −10% variation) to 0.0388 s (real power at +10% variation). The overshoot ranged from 21.28% (voltage at −10%) to 32.03% (real power at +10%). The grid frequency remained largely unaffected, with a maximum settling time of 8.002×10^{-4} s and a maximum overshoot of only 1.84%. These results demonstrate the high reliability and robustness of the proposed controller under parameter uncertainties.

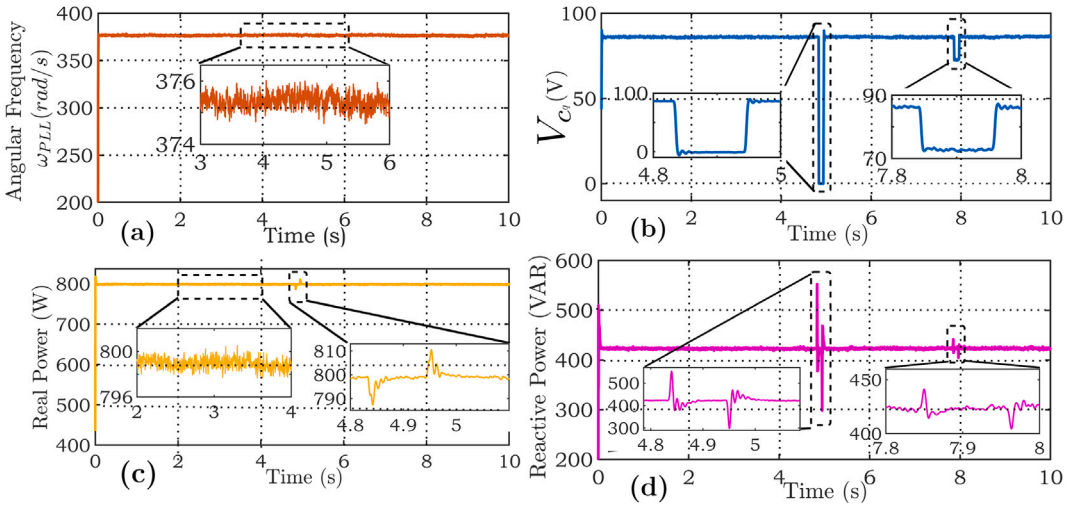

Fig. 7. Performance of the FOPI-based model under LVRT and voltage sag condition: (a) Angular frequency ω_{PLL}, (b) q-Axis voltage v_{c_q}, (c) Real power P, and (d) Reactive power Q.

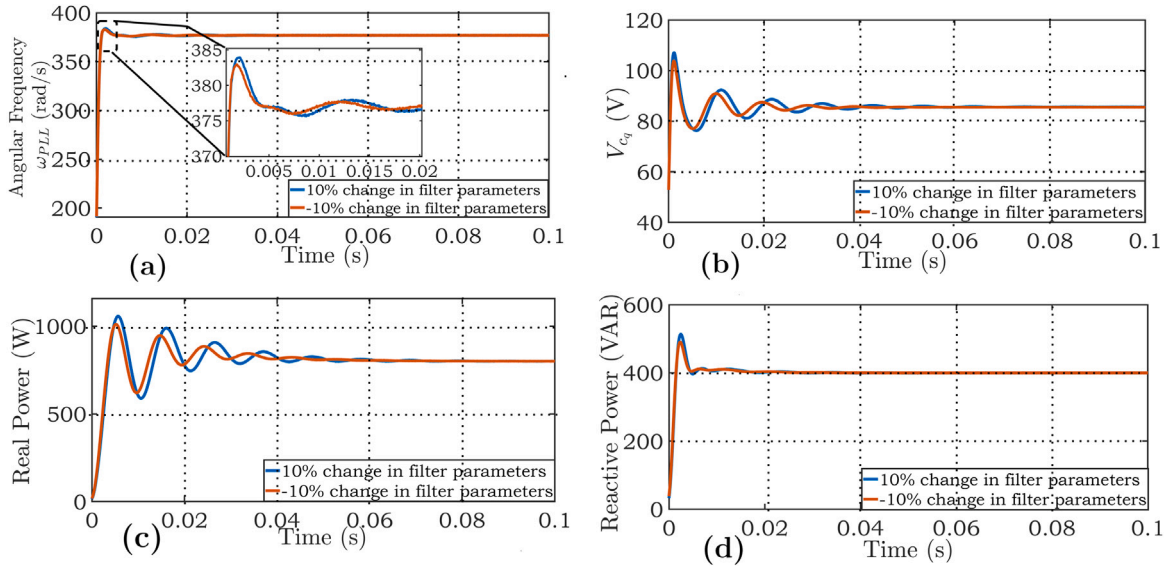

Fig. 8. Performance of the FOPI-based model under ±10% variation in parameters: (a) Angular frequency ω_{PLL}, (b) q-axis voltage v_{c_q}, (c) Real power P, and (d) Reactive power Q.

Altogether, the proposed system exhibited rapid stabilization with minimal transient degradation and maintained all response variables within acceptable limits, confirming its robust stability.

7. Conclusion and future research

In this work, a high-fidelity FOPI control model for grid-connected inverters is developed using the M-SBL fitting method to convert fractional dynamics into precise integer order equivalents. Five FOPI controllers, whose fractional orders are optimized by a genetic algorithm in 50 iterations, reduce transient tracking error by 25.36% compared to conventional PI control while maintaining robust performance under dynamic load and voltage disturbances. Further, a small signal model was derived, which decreases simulation time by more than five times relative to the full nonlinear inverter representation. Stability analysis was performed to confirm all eigenvalues lie in the left half-plane; further, the modal evaluation identifies four critically damped, one heavily damped, and four underdamped modes and the Lyapunov direct method verifies asymptotic convergence. Real-time OPAL-RT experiments validate these theoretical findings under multiple realistic scenarios. In the future, the approach can be extended to multi-inverter systems and alternative inverter architectures—including the grid forming converters, virtual synchronous generators, and renewable energy interfaces. Future work can explore the application of MSBL for more advanced fractional controllers such as FOPID, resilient tri-parametric FO controllers, FO PI–PD, along with FO active disturbance rejection control, and FO sliding mode control, etc. Moreover, real-time implementation and validation using platforms like OPAL-RT will be pursued to assess the practical feasibility and robustness of the proposed controller under communication delays and cyber–physical disruptions.

CRediT authorship contribution statement

Muhammad Ahsan Zamee: Formal analysis, Data curation, Conceptualization. **Afaq Hussain:** Software, Methodology, Investigation. **M.J. Hossain:** Supervision.

Declaration of competing interest

The authors declare that there are no conflicts of interest amongst the authors regarding the publication of this article.

Appendix

Controller gains: $k_p^P, k_p^Q = 0.50$, $k_i^P, k_i^Q = 25$, $k_p^{c_d}, k_p^{c_q} = 1$, $k_i^{c_d}, k_i^{c_q} = 100$, $k_p^{PLL} = 0.25$, $k_i^{PLL} = 2$, **System parameters:** $L_i = 4.20$ mH, $L_g = 0.50$ mH, $C_i = 15$ µf, $\omega_c = 50.26$ rad/s, $R_f = 0.30$ Ω, $R_g = 0.1$ Ω, $R_c = 2$ Ω, $\omega_g = \omega_{PLL} = 377$ rad/s, $V_{b_{Q_{nom}}} = 85.0$ V.

Data availability

Data will be made available on request.

References

[1] Y. Wu, H. Wu, F. Zhao, Z. Li, X. Wang, Influence of PLL on stability of interconnected grid-forming and grid-following converters, IEEE Trans. Power Electron. (2024).

[2] S.T. Meraj, S. Yu, K. Hasan, H. Trinh, P. Shi, An advanced frequency adaptive PLL for grid connected inverters under abnormal grid conditions, IEEE Trans. Ind. Appl. (2024).

[3] E.A. Ducoin, Y. Gu, B. Chaudhuri, T.C. Green, Analytical design of contributions of grid-forming & grid-following inverters to frequency stability, IEEE Trans. Power Syst. (2024).

[4] M. Jamali, M.S. Sadabadi, M. Davari, A set-theoretic adaptive current control design for grid-following inverter-based resources to tackle practically non-ideal control inputs, IEEE Trans. Autom. Sci. Eng. (2025).

[5] J. Wijesingha, L. Meegahapola, X. Yu, Performance analysis of active/reactive power control of a grid following voltage source inverter using sliding mode control, in: 2024 IEEE 34th Australasian Universities Power Engineering Conference, AUPEC, IEEE, 2024, pp. 1–6.

[6] J.K. Singh, K. Al Jaafari, R.K. Behera, K. Al Hosani, U.R. Muduli, Faster convergence controller with distorted grid conditions for photovoltaic grid following inverter system, IEEE Access 10 (2022) 29834–29845.

[7] Y. Yu, Y. Guan, W. Kang, J. Wu, J.C. Vasquez, J.M. Guerrero, Active damping of grid-forming voltage-source converter using fractional-order regulators, IEEE Trans. Ind. Electron. (2025).

[8] L.L. Chiza, D. Benítez, R. Aguilar, O. Camacho, Droop control in grid-forming converters using a fractional-order pi controller: A power system transient analysis, Results Control. Optim. 18 (2025) 100517.

[9] R. Rosso, S. Engelken, M. Liserre, Robust stability investigation of the interactions among grid-forming and grid-following converters, IEEE J. Emerg. Sel. Top. Power Electron. 8 (2) (2019) 991–1003.

[10] H. Zamani, K. Abbaszadeh, M.H. Karimi, J. Gyselinck, Adaptive model predictive control for LCL-filter grid-tied inverters, IEEE Trans. Ind. Electron. (2023).

[11] Y. Li, Y. Gu, T.C. Green, Revisiting grid-forming and grid-following inverters: A duality theory, IEEE Trans. Power Syst. 37 (6) (2022) 4541–4554.

[12] M.R. Kumar, S. Ghosh, Hybrid optimization based fopi controller design with real-time validation, IFAC- Pap. 51 (1) (2018) 78–83.

[13] M. Boudana, S. Ladaci, J.-J. Loiseau, Fractional order PIλdμ control design for a class of cyber-physical systems with fractional order time-delay models: fractional PIλdμ design for CPS with time-delay models, Int. J. Cyber- Phys. Syst. (IJCPS) 1 (2) (2019) 1–18.

[14] M.M. Hadji, S. Ladaci, State space feedback control with fractional order PI configuration for fractional order cryptovirology stabilization in blockchain systems, in: 2022 19th International Multi-Conference on Systems, Signals & Devices, SSD, IEEE, 2022, pp. 1009–1013.

[15] H. Bouyedda, S. Ladaci, H. Schulte, Cruise control design for an electric vehicle using a fractional order PI λ d μ with genetic algorithms optimization, in: 2019 8th International Conference on Systems and Control, ICSC, IEEE, 2019, pp. 158–163.

[16] R. Meena, S. Chakraborty, V.C. Pal, H. Lala, Experimentally validated fractional-order PI with anti-windup for fractional-order plus time delay processes, Int. J. Dyn. Control. 12 (12) (2024) 4232–4243.

[17] J.M. Ribeiro, M.F. Santos, M. Carmo, M. Silva, Comparison of PID controller tuning methods: analytical/classical techniques versus optimization algorithms, in: 2017 18th International Carpathian Control Conference, ICCC, IEEE, 2017, pp. 533–538.

[18] V. Reis, M. Santos, M. Carmo, F. Ferreira, Control of level systems by arduino via PC platform, in: 2016 20th International Conference on System Theory, Control and Computing, ICSTCC, IEEE, 2016, pp. 251–256.

[19] B.L.G. Costa, J.P.L.S. de Almeida, B.A. Angélico, Application of optimization heuristics in tuning decentralized pid controllers, in: 2012 10th IEEE/IAS International Conference on Industry Applications, IEEE, 2012, pp. 1–8.

[20] A.M. AbdelAty, A. Al-Durra, H. Zeineldin, E.F. El-Saadany, Improving small-signal stability of inverter-based microgrids using fractional-order control, Int. J. Electr. Power Energy Syst. 156 (2024) 109746.

[21] F.N. Deniz, B.B. Alagoz, N. Tan, M. Koseoglu, Revisiting four approximation methods for fractional order transfer function implementations: Stability preservation, time and frequency response matching analyses, Annu. Rev. Control. (ISSN: 1367-5788) 49 (2020) 239–257.

[22] A. Charef, H. Sun, Y. Tsao, B. Onaral, Fractal system as represented by singularity function, IEEE Trans. Autom. Control 37 (9) (1992) 1465–1470.

[23] P. Aryan, G.L. Raja, U. Mehta, T.R. Chelliah, U.R. Muduli, A resilient tri-parametric fractional frequency control for cybersecurity threats amid latency, IEEE Trans. Ind. Appl. (2025) 1–15, http://dx.doi.org/10.1109/TIA.2025.3546173.

[24] U. Mehta, P. Aryan, G.L. Raja, Tri-parametric fractional-order controller design for integrating systems with time delay, IEEE Trans. Circuits Syst. II: Express Briefs 70 (11) (2023) 4166–4170, http://dx.doi.org/10.1109/TCSII.2023.3269819.

[25] R. Mondal, J. Dey, A novel design methodology on cascaded fractional order (FO) PI-pd control and its real time implementation to cart-inverted pendulum system, ISA Trans. (ISSN: 0019-0578) 130 (2022) 565–581, http://dx.doi.org/10.1016/j.isatra.2022.04.015, URL https://www.sciencedirect.com/science/article/pii/S0019057822001768.

[26] M. Rasheduzzaman, J.A. Mueller, J.W. Kimball, An accurate small-signal model of inverter- dominated islanded microgrids using dq reference frame, IEEE J. Emerg. Sel. Top. Power Electron. 2 (4) (2014) 1070–1080.

[27] J.A. Mueller, M. Rasheduzzaman, J.W. Kimball, A model modification process for grid-connected inverters used in islanded microgrids, IEEE Trans. Energy Convers. 31 (1) (2016) 240–250.

[28] J. Mueller, Small-Signal Modeling of Grid-Supporting Inverters in Droop Controlled Microgrids, Department of Electrical and Computer Engineering, Missouri University of Science and Technology, Rolla, MO, USA, 2014.